A New Robust Frontal Disturbance Index of the Oyashio Extension Sea Surface Temperature Front

RICHARD J. HALL,[a] ARNAUD CZAJA,[a] GOKHAN DANABASOGLU,[b] CLARA DESER,[b] CLAUDE FRANKIGNOUL,[c,d] AND YOUNG-OH KWON[c]

[a] *Department of Physics, Imperial College, London, United Kingdom*
[b] *National Center for Atmospheric Research, Boulder, Colorado*
[c] *Woods Hole Oceanographic Institution, Woods Hole, Massachusetts*
[d] *LOCEAN, Sorbonne Université/IRD/CNRS/MNHN, Paris, France*

(Manuscript received 24 October 2023, in final form 26 September 2024, accepted 6 November 2024)

ABSTRACT: The Oyashio Extension (OE) frontal zone in the northwest Pacific Ocean is associated with strong gradients of sea surface temperature (SST) and salinity. The OE front enhances baroclinicity and anchors the storm tracks; changes in its position and strength may impact atmospheric variability. North–south shifts in the OE front are often defined using the leading principal component for the latitude of the absolute maximum SST gradient in the northwest Pacific (145°–170°E), the so-called Oyashio Extension index (OEI). We show that the OEI is sensitive to the choice of SST dataset used in its construction, and that the significance of regressions of atmospheric fields onto the OEI also depends on the choice of SST datasets, leading to nonrobust results. This sensitivity primarily stems from the longitudinal domain used to define the OEI including a region with parallel or indistinct frontal zones in its central section (155°–164°E), leading to divergent results across datasets. We introduce a new index that considers the extent to which the SST front across this central section departs from climatology, the frontal disturbance index (FDI). For the months considered and over short time lags, the FDI produces more consistent results on air–sea interactions and associated high-frequency storm-track metrics than the conventional OEI, with a southward shift of the storm track for a more positive FDI. The FDI appears to be related to oceanic mesoscale eddy activity in the central OE region. There are significant asymmetric associations between the FDI and storm-track metrics dependent on the sign of the FDI.

SIGNIFICANCE STATEMENT: In this study, we aim to understand how the choice of dataset may influence the interpretation of interactions between the ocean and the overlying atmosphere near sea surface temperature (SST) fronts. We find that using different SST datasets affects the results, due to slight differences in the representation of the location of the maximum SST gradient. To understand this, we develop a new index which relates to the degree of disturbance of the SST front. The new index produces regression results that are more consistent across the different datasets. We also identify some possible links between the frontal disturbance and the presence of ocean eddies. We advise that the sensitivity to dataset choice is given due consideration in regions near SST fronts.

KEYWORDS: Atmosphere-ocean interaction; Fronts; Sea surface temperature; Regression analysis

1. Introduction

Oceanic western boundary currents (WBCs) transport significant quantities of heat eastward and poleward in both the North Atlantic and Pacific Oceans. In the Atlantic, the WBC is the Gulf Stream, while in the Pacific, the configuration is different: to the south is the Kuroshio, while to the north and forming part of the subpolar gyre is the Oyashio (Qiu 2019). Both currents turn eastward away from the coast of Japan and into the Pacific basin where they are known as the Kuroshio Extension (KE) and Oyashio Extension (OE; also sometimes referred to as the subarctic current or front), located at around 35° and 41°N, respectively (Kwon et al. 2010). The OE is associated with strong gradients of sea surface temperature (SST) and salinity, whereas the KE is more clearly defined by a gradient in sea surface height (SSH) (Qiu et al. 2017; Zhou and Cheng 2021). These features are shown schematically in Fig. 1. The region is complex, with several diverging and converging currents between the two extensions (Kida et al. 2015; Yasuda 2003).

The strong meridional gradients of SST in the OE region may act to enhance baroclinicity and anchor the storm track in the overlying atmosphere (Hoskins and Valdes 1990; Nakamura et al. 2008) and have been the focus of numerous observational and modeling studies concerning air–sea interactions (Kwon et al. 2010; Frankignoul et al. 2011; Taguchi et al. 2012; Smirnov et al. 2015; Révelard et al. 2016, 2018). Air–sea heat fluxes associated with mesoscale air–sea interaction are robust in the vicinity of WBCs (Seo et al. 2023). The SST signal from mesoscale processes such as eddies and SST fronts

Denotes content that is immediately available upon publication as open access.

Supplemental information related to this paper is available at the Journals Online website: https://doi.org/10.1175/JCLI-D-23-0642.s1.

Corresponding author: Richard J. Hall, rjhall@imperial.ac.uk

DOI: 10.1175/JCLI-D-23-0642.1

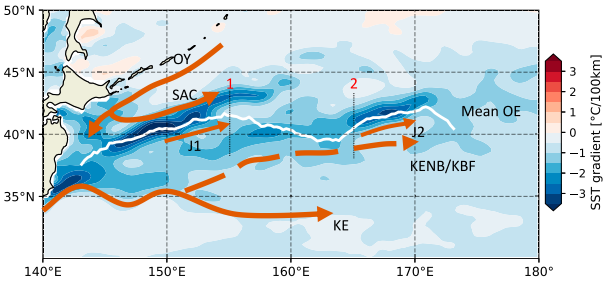

FIG. 1. Schematic of the location of fronts referred to in the text. KE: Kuroshio Extension; KENB/KBF: Kuroshio Extension Northern Branch/Kuroshio Bifurcation Front; OY: Oyashio Current; SAC: Subarctic Current; OE: Oyashio Extension (143°–173°E; shown in white); J1, J2: Isoguchi jets. Background field is the mean DJFM meridional SST gradient from the Reynold optimally interpolated (OI) SST dataset. Meridional lines (1 and 2) mark the longitudinal segment within the OE used to calculate the FDI (155°–164°E). Data are not detrended.

modifies the surface turbulent heat and momentum fluxes and causes local responses in the marine atmospheric boundary layer (Small et al. 2008). This in turn drives a nonlocal response in the storm track (e.g., Czaja et al. 2019; Seo et al. 2023). A poleward decrease in sensible heat flux across the frontal zone sustains the strong near-surface baroclinicity against the relaxing effect of strong poleward eddy heat transport (Sampe et al. 2010).

A better understanding of the nature of SST variability and associated air–sea interactions along oceanic frontal zones will improve the process-level understanding of ocean-to-atmosphere feedbacks as well as the performance of model simulations. Crucial questions are the extent to which air–sea interactions over the OE region influence the wider atmospheric circulation and how this depends on the sharpness and location of the SST gradient and magnitude of the associated SST anomalies more generally (Small et al. 2019). Many modeling studies (e.g., Smirnov et al. 2015; Ma et al. 2017; Kuwano-Yoshida and Minobe 2017; Yook et al. 2022) impose observed SST anomalies in the Kuroshio–Oyashio Extensions (KOE) region in an atmospheric model to investigate causal linkages. The atmospheric response may depend on the spatial resolutions both of the model and of the imposed SST anomalies. Only when the model has sufficient horizontal resolution can the full impact of mesoscale forcing by SST fronts on the storm track be correctly simulated (e.g., Smirnov et al. 2015; Ma et al. 2017).

To address these questions concerning air–sea interactions, there must be high confidence in determining the location and shifts in these SST frontal zones and the nature of the associated SST anomalies. Frankignoul et al. (2011) developed an OE index (OEI) based on the location of the maximum SST gradient in the OE region (145°–170°E), which has been used in a number of subsequent studies (e.g., Smirnov et al. 2015; Qiu et al. 2017; Wu et al. 2018; Yao et al. 2018a,b). Frankignoul et al. (2011) identified that north–south shifts in the SST front were associated with large-scale atmospheric responses up to 3 months later. Subsequent work (Qiu et al. 2017) concluded that the western (145°–153°E) and eastern (153°–173°E) sections of the OEI were in fact uncorrelated on a synchronous basis over a range of different time scales, although lagged relationships did occur. The different sections of the front were driven by different physical mechanisms (Wu et al. 2018) and were associated with different SST anomaly patterns. Other studies identify SST frontal indices based on simple regional anomalies, although these are often applied to the general KOE region (e.g., 36°–42°N, 140°–171°E) and may provide different information about air–sea interactions that are not necessarily connected to shifts in SST fronts (e.g., Taguchi et al. 2012; Wills and Thompson 2018). It is also possible to identify SST fronts from SST gradients using pixel-based high-resolution satellite images at daily resolution (Wang et al. 2021).

The reliability of analyses of SST-front-driven air–sea interactions depends on the ability of SST datasets to accurately represent the SST front. New high-resolution gridded SST datasets are available, with horizontal resolutions commonly of 0.25° in latitude and longitude or higher. The credibility of these SST products depends upon the availability of observations and the gridding procedure used (Huang et al. 2021). Gridded SST datasets capture large-scale modes of variability such as El Niño–Southern Oscillation (ENSO) with high correlations between time series derived from different datasets (Yang et al. 2021). However, at the scale of SST fronts, the sharpness of a front in the dataset is not necessarily proportional to the grid resolution used (Martin et al. 2012; Fiedler et al. 2019). These differences are related to distinctive retrieval and interpolation methods and interpolation grid size and bias correction of input data (Yang et al. 2021).

We are therefore motivated to calculate the OEI for a range of SST datasets to determine first their level of agreement and second to identify whether the differences impact significantly on the interpretation of air–sea interactions. We focus on late winter (January–March) as turbulent heat fluxes are stronger in winter and the mean position of the storm track is collocated with oceanic fronts in winter but not in summer (Nakamura et al. 2004). We also investigate whether any discrepancies in the OEI have any physical basis. We find that the OEI interaction with atmospheric variables is dataset dependent. This leads us to develop a new index, the frontal disturbance index (FDI). The data used are described in section 2, and methods are explained in section 3. Section 4 presents our results, and section 5 is a discussion and summary of our findings.

2. Data

Reliable high-resolution SST datasets which resolve mesoscale processes are required. One option is to obtain these from the newest generation of gridded observational datasets, with increased temporal and spatial resolution. The National Oceanic and Atmospheric Administration (NOAA) optimum-interpolated (OI) SST, version 2.1, dataset (Reynolds et al. 2007; Banzon et al. 2016; Huang et al. 2021) is available at daily resolution on a 0.25° grid from 1981 to the present for the Advanced Very High-Resolution Radiometer (AVHRR)-

only product. The Operational Sea Surface Temperature and Sea Ice Analysis (OSTIA) dataset (Donlon et al. 2012; Good et al. 2020) is available from October 1981 onward at a daily resolution on a 0.05° grid. In addition, we use the Group for High-Resolution SST Multi-Product Ensemble (GMPE, Martin et al. 2012; Fiedler et al. 2019) analysis for 1981–2016 at daily resolution on a 0.25° grid. The GMPE uses an ensemble of six high-resolution products (including OSTIA and OI; Fiedler et al. 2019) and takes the ensemble median value for each grid box, having regridded the data to a common grid. Details of the method are described by Martin et al. (2012). We also compare these products to the SSTs in the ERA5 reanalysis (Hersbach et al. 2020), available on a 0.25° grid with an hourly time step from 1940 onward. ERA5 uses Hadley Centre Sea Ice and Sea Surface Temperature dataset, version 2.1.0 (HadISST2.1.0), for the period to 2007 (at 5-day and 1° resolutions; J. J. Kennedy 2023, personal communication) and OSTIA thereafter. None of these datasets are independent, as they use many of the same satellite and in situ data sources; however, they are selected as being representative of typical datasets that may be used in the analysis of air–sea interactions. We calculate monthly means of daily data for the common period January 1982–December 2016, regridding to a common 0.25° grid. The OEI and FDI are calculated separately for each SST dataset (see section 3). While this regridding enables a better comparison of datasets, the actual resolutions are still different and will reflect the original data assimilation and interpolation schemes: a highly interpolated dataset will lose spatial resolution, with a smoothing out of mesoscale patterns. The use of low-resolution SST data in reanalyses means that the SST frontal impacts on the atmosphere may be underestimated (Zhou and Cheng 2021).

Atmospheric and surface flux variables [sea level pressure (SLP), meridional wind, temperature, total precipitation, and vertical velocity (omega)] at 0.25° horizontal resolution are obtained from the ERA5 reanalysis, to assess the impact of different OEI and FDI indices on storm-track variability. SSH data are obtained from the Copernicus Marine Environment Monitoring Service (CMEMS). This is an altimeter satellite product available as gridded data at 0.25° and daily resolution, from 1993 (https://doi.org/10.48670/moi-00148).

3. Methods

a. Definition of the Oyashio Extension Index (OEI)

Following Frankignoul et al. (2011), we calculate the OEI as the monthly standardized principal component (PC) time series for the first empirical orthogonal function (EOF) of the latitude of the absolute maximum meridional SST gradient for the September–April period, based on the monthly SST data. This period is chosen to avoid the summer season because the summer SST gradient has different characteristics. We identify the latitude of the maximum SST gradient at each longitude over the OEI region at each time step but restrict the EOF calculation domain to the eastern part of the region (35°–47°N, 153°–173°E) following Qiu et al. (2017). We detrend the latitude of maximum SST gradients using a third-order polynomial fit for the 1982–2016 period to remove low-frequency variability that may bias the results, and the mean seasonal cycle is removed by subtracting the climatological monthly means prior to the calculation of the EOF.

Based on the monthly OEIs calculated from each dataset as above, three additional versions of the OEI are calculated for the December–March (DJFM) seasonal window: 1) monthly, 2) seasonal mean, and 3) monthly intraseasonal (anomalies from the seasonal mean for each year). These indices allow us to compare how similar the indices are at different temporal resolutions. The OEIs from different datasets for each of these versions are compared by computing pairwise correlation coefficients, and a time series of average pairwise differences (the "difference index") is calculated for the September–April monthly time series.

b. Definition of the FDI

The OE SST front is relatively weak and diffuse in the central portion of the domain (Fig. 1). To assess the extent to which the location of OE front departs from the climatology across this section, we compute a FDI as follows. First, we calculate the detrended (third-order polynomial fit) standardized anomaly of the latitude of the SST front F as the latitude of the maximum SST gradient ϕ as a function of longitude λ and time ($t = 1, \ldots, N$) within 155°–164°E:

$$F_{t,\lambda} = \frac{\phi_{t,\lambda} - \overline{\phi}_{\lambda}}{\sqrt{\frac{1}{N-1}\sum_{t=1}^{N}(\phi_{t,\lambda} - \overline{\phi}_{\lambda})^2}}, \tag{1}$$

where the overbar denotes time mean. Then, we find the root-mean-square deviation of these standardized anomalies with respect to longitude ($l = 1, \ldots, M$):

$$\mathrm{FDI}_t = \sqrt{\frac{1}{M}\sum_{\lambda=1}^{M} F_{t,\lambda}^2}. \tag{2}$$

Higher FDI values indicate a higher overall departure from the climatological time mean.

A schematic diagram of the FDI calculated for synthetic data is shown in Fig. 2. Here, the climatology has an FDI value of zero, the minimum possible. The FDI is proportional to the absolute magnitude of the mean displacement from climatology (red and blue lines have equal FDI values but are on opposite sides of the climatology; the gray line has a higher FDI as it is further from the climatological front). The green line is zonal in orientation but has an FDI of 4.5 as it intersects climatology at an angle, with increasing differences further from the intersection. The two stepped lines are the reverse of each other. However, their FDIs are different; for the orange line, the step down is broadly aligned with climatology, whereas in the purple line, as climatological values decrease eastward, the step broadly increases in latitude. These examples show that the FDI captures both absolute departures from the time-mean latitude, and the extent to which the maximum SST gradient makes large latitudinal jumps between adjacent longitudes, although this is also dependent on

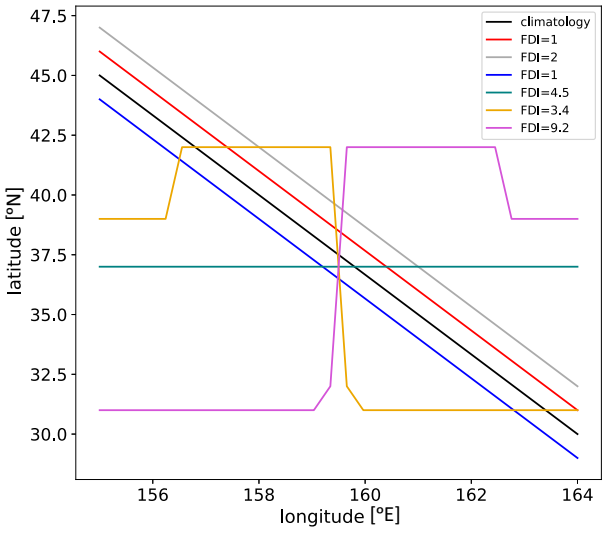

FIG. 2. Diagram of synthetic data simulating different locations of maximum SST gradients, over the longitude and latitude range of the central section of the OE (155°–164°E). The synthetic climatological maximum SST gradient is shown by the bold black line, and five different synthetic gradient locations are shown, together with the FDI value for each.

the alignment of the jump with the angle of the climatological SST front.

In the SST datasets analyzed here, the range of FDI values is around 0.3–1.9. For use in asymmetric regression, we remove the climatological monthly mean FDI from the time series, and thus the large negative FDI values indicate the frontal positions close to climatology.

c. *Other calculations*

To assess physical mechanisms that might be linked to the FDI, we isolate oceanic mesoscale features (including coherent eddies) in the region 150°–170°E, 30°–50°N. We use a two-dimensional fast Fourier transform (FFT) spatial filter to isolate high and low wavenumbers in the SST data. We filter daily data using a filter length scale of 420 km as a cutoff (wavenumber equal to 0.0024 km^{-1}) to separate eddy length scales from larger scales and then calculate the monthly standard deviation of the resulting data. The high-pass filter isolates the mesoscale eddies but produces a field with a lot of noise. To identify any large-scale patterns in the mesoscale eddies, we additionally apply a FFT low-pass spatial filter with the same cutoff as the high-pass filter to the monthly standard deviation fields of the high-pass data. For full details of the method used, see Sroka et al. (2022). For comparison, we also calculate daily surface eddy kinetic energy from the SSH according to

$$\text{EKE} = \frac{1}{2}(u_g'^2 + v_g'^2) = \frac{1}{2}\left[\left(-\frac{g}{f}\frac{\partial h'}{\partial y}\right)^2 + \left(\frac{g}{h}\frac{\partial h'}{\partial x}\right)^2\right], \qquad (3)$$

where u_g' and v_g' are the zonal and meridional components of the geostrophic current anomaly, respectively; f is the Coriolis parameter, g is the gravitational acceleration; h' are the daily SSH anomalies from the climatological mean; and y and x are distances along the latitudinal and longitudinal directions, respectively. No spatial filtering is applied to (3). A monthly mean EKE is calculated, detrended with a third-order polynomial trend.

We calculate the monthly standard deviation of 8-day high-pass-filtered 500-hPa vertical velocity (omega) by applying a four-point high-pass Butterworth filter to the daily data, isolating variability at the synoptic time scale. This can give an indication of storm-track activity, increased variance being associated with passage of low pressure systems, where enhanced upward and downward vertical velocities can occur in different locations within the same system, associated with warm and cold sectors and fronts. We also calculate the 850-hPa meridional heat flux ($v'T'$) and 300-hPa wind variance ($v'v'$), where v' and T' are the 2–8-day bandpass-filtered meridional wind and temperature using a four-point Butterworth filter. We also calculate indicators of surface storm tracks, using an alternative high-pass filtering approach involving daily differencing (Wallace et al. 1988). We apply this to 850-hPa meridional wind and total precipitation. In addition, the Eady growth rate (EGR) at 800 hPa is calculated according to

$$\text{EGR} = -0.31\ \frac{g}{N\theta_o}\frac{\partial \theta}{\partial y}, \qquad (4)$$

where N is the buoyancy frequency, θ is the potential temperature, and θ_o is the climatological monthly mean temperature (e.g., Small et al. 2014). The EGR is an important measure for identifying baroclinic eddy development (e.g., Hoskins and Valdes 1990).

At the mesoscale in WBC regions, there is a local atmospheric response in the marine atmospheric boundary layer. These responses can then drive nonlocal responses in the extratropical storm tracks (Czaja et al. 2019; Seo et al. 2023). We identify these large-scale atmospheric responses associated with the OEI and FDI by regressing the different atmospheric variables on the monthly time series. We use both conventional symmetric linear regression and asymmetric regression to accommodate potential nonlinear associations with respect to the sign of the index (e.g., Révelard et al. 2016). The asymmetric regression method is described in detail in Frankignoul and Kwon (2022). Negative and positive values of the index (recall the FDI is adjusted by removal of the climatological mean, creating positive and negative values) are regressed separately against the relevant time steps of the detrended anomaly field, having first removed the time mean for negative and positive index values, separately, from each set of data to provide an unbiased estimate. Statistical significance for regressions is determined using the Wald test (similar to the Student's t test; Wald 1943), and we present results for two levels of significance ($p < 0.1$, $p < 0.2$). We use the false discovery rate (FDR; Benjamini and Hochberg 1995; Wilks 2016) to compensate for spatial autocorrelation and multiple hypothesis testing and the overinterpretation of results through the reporting of spurious significant p values.

TABLE 1. Pearson correlations between the PC-based OEI time series for different SST datasets and for different temporal resolutions. All correlations are calculated for 1982–2016. All correlations are significant ($p < 0.05$).

Correlation	SONDJFMA separate months	DJFM separate months	DJFM seasonal mean	DJFM subseasonal anomalies
ERA5 vs OI	0.72	0.62	0.69	0.49
ERA5 vs GMPE	0.71	0.61	0.71	0.46
ERA5 vs OSTIA	0.71	0.57	0.75	0.24
OI vs GMPE	0.81	0.78	0.88	0.58
OI vs OSTIA	0.80	0.72	0.77	0.53
GMPE vs OSTIA	0.78	0.72	0.86	0.41

4. Results

a. *The sensitivity of the OEI to choice of dataset*

Correlations between the OEIs show considerable variation between dataset pairs and depend on the temporal window and resolution used (Table 1).

The correlations are higher for the September–April monthly resolution time series than for the extended winter (DJFM) monthly series, indicating weaker correlations in the winter months.

Correlations for DJFM seasonal means are quite high (0.69–0.88), while those for subseasonal anomalies are lower (0.24–0.58). The correlations for time series of separate DJFM months lie somewhere in between. Correlations with ERA5 and other datasets are generally lower than those between other dataset pairs.

The September–April (SONDJFMA) OEI with monthly resolution shows good agreement across datasets at multiannual time scales (Fig. 3a), while the difference index shows that there can be considerable disagreements on monthly time scales (Fig. 3b). Over the September–April window, there are lower correlations between ERA5 and the other datasets in the winter months (generally February and March, Fig. 3c). The lower ERA5 correlations in February and March are also present in the subseasonal anomalies, although here the correlations are even lower, with increased noise in the datasets at subseasonal time scales (Fig. 3d). These correlation statistics suggest that the OEI may be most suitable for use with DJFM seasonal means for calculating interannual variability.

When atmospheric and SST fields are regressed on these different OEIs, the results are inconsistent across the datasets, leading to concerns regarding interpretation when a single dataset is used (Fig. S1 in the online supplemental material). However, this sensitivity stems from the differences in the OEIs rather than the regression fields. Hence, if OEI time

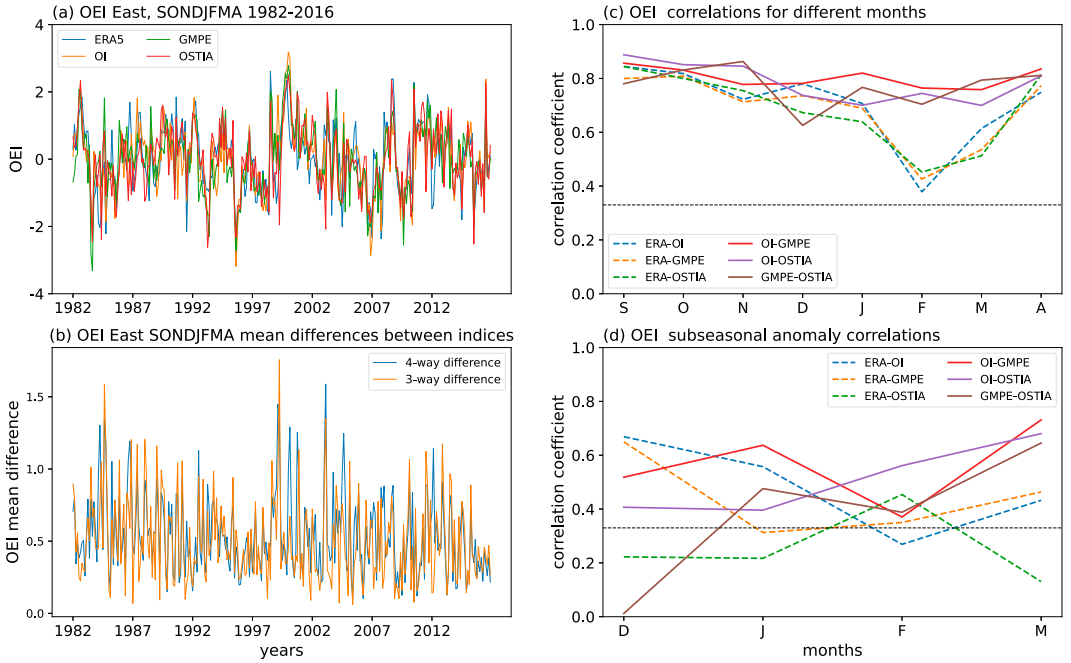

FIG. 3. (a) The OEIs (eastern section; 153°–173°E) for SONDJFMA with monthly resolution based on the four different SST datasets and (b) the mean absolute difference between the indices, calculated between all indices (four-dataset difference) and without ERA5 (three-dataset difference). (c) Interannual correlations between OEIs for each month in the window SONDJFMA based on different pairs of SST datasets. (d) As in (c), but for the subseasonal anomalies in DJFM. In (c) and (d), correlations between ERA5 and other datasets are shown as dashed lines and the horizontal dashed lines denote the significance threshold for $p < 0.1$.

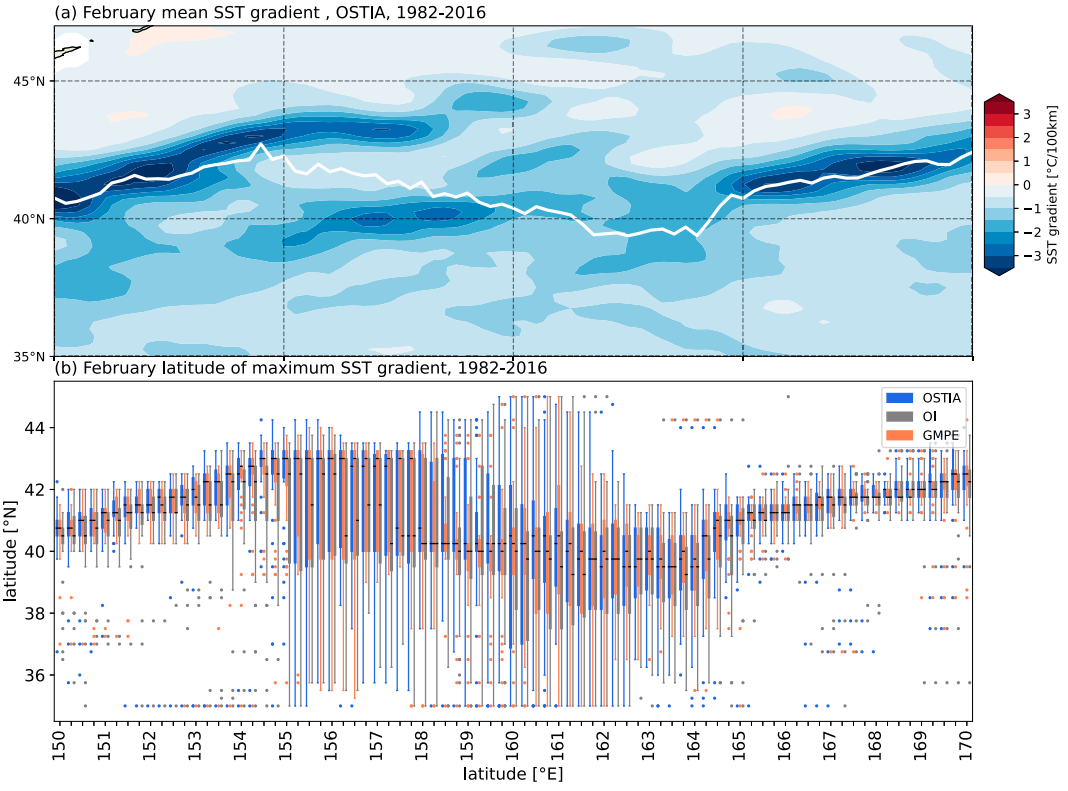

FIG. 4. (a) Spatial pattern of the February mean SST gradient from OSTIA for 1982–2016. White line shows the February climatological absolute maximum SST gradient. (b) Box-and-whisker plots showing the February latitudinal distribution of the maximum poleward absolute SST gradient at each longitude, for each dataset for 1982–2016 (OSTIA in blue, OI in gray, and GMPE in orange). The central box at each longitude shows the IQR, and the horizontal black line indicates the median. The whiskers extend from each box by 1.5 times the IQR, and dots indicate values that occur outside these ranges.

series and SST datasets are swapped, so that, for example, the OI SST is regressed on the ERA5 OEI, the same spatial patterns of regression coefficients are obtained as that when regressing the ERA5 SST on the ERA5 OEI.

From the results shown in Fig. 3, ERA5 seems to be an outlier in that it disagrees with other SST datasets considered. Thus, we do not consider this SST product further in the subsequent analysis.

b. Reasons for OEI discrepancies

Here, we investigate the differences in the OEI across datasets to identify their origin, focusing on the complex spatial structure of SST gradients within the OE region.

The February-mean SST gradient pattern for the OSTIA dataset is shown in Fig. 4a. The region does not contain a single continuous front: there are parallel fronts, single well-defined fronts, and regions where the front is poorly defined. Other datasets have very similar patterns (Fig. S2), and other months are qualitatively similar (not shown).

The latitudinal occurrences of absolute maximum poleward SST gradients shown for February (Fig. 4b) illustrate these distinct regions. Within 150°–155°E and 165°–170°E, there are strong, well-defined SST gradients corresponding to the locations of the Isoguchi jets (Isoguchi et al. 2006; Kida et al. 2015; J1 and J2 in Fig. 1). These quasi-stationary geostrophic jets transport warm water poleward. This explains their consistent representation among the datasets and the relatively narrow interquartile ranges (IQRs) in Fig. 4b. However, within 155°–165°E, the pattern of SST gradients is more complex. Two parallel SST gradient fronts are evident from 155° to 160°E [one near 40°N and the other near 43°N (Fig. 4a and Fig. S2)]. The broad IQRs on the boxplots here indicate sampling of the maximum SST gradient from both regions of strong SST gradients (Fig. 4b), with datasets showing different preferred latitudes at different longitudes and times. While OSTIA and GMPE show a skewed distribution with more frequent sampling of the northern front, the median value for OI is located further south, particularly between 156° and 157°E, indicating that the maximum SST gradient occurs more frequently along the more southern SST gradient region in OI. At around 159°E, OSTIA has a much wider IQR than either OI or GMPE. Between 160° and 164°E, there is a more diffuse front, with fragmented sections of stronger and weaker gradients. In February, this zone of weak overall gradients is broadest latitudinally and may contribute to the low correlations in OEI time series in February (Figs. 3c,d), although it is evident in other months. Some of the differences between the OEIs arise from the central section: either slight differences in the representations of the relative strengths of the parallel fronts

TABLE 2. Pearson correlations between the FDI time series for 155°–164°E for different datasets and time steps. All correlations are over the 1982–2016 period, and all correlations are significant ($p < 0.05$).

Correlation	SONDJFMA separate months	DJFM separate months	DJFM seasonal mean	DJFM subseasonal anomalies
OI-GMPE	0.61	0.55	0.56	0.55
OI-OSTIA	0.76	0.69	0.67	0.55
GMPE-OSTIA	0.64	0.62	0.77	0.40

in its western half means that different latitudes are selected by the datasets, or over the diffuse, shallow front in the eastern half, small differences in gradient strength could result in large latitudinal discrepancies between datasets. Other months are qualitatively similar and display the same regions of discrepancies (not shown).

c. *OE variability and frontal disturbance for 155°–164°E*

We now examine the central section of the OE SST front, using the FDI calculated over 155°–164°E. This longitude range comprises just under half the length of the OE used to calculate the eastern OEI (153°–173°E). Recall that a high FDI indicates the OE front has a large departure from climatology, whereas the smaller the value is, the closer the front is to climatology. The correlations between the GMPE and other FDI time series from different datasets, at different temporal resolutions, are not as strong as those obtained from the OEI, except for the DJFM subseasonal anomalies which are of similar magnitude (Table 2, compared with Table 1). This may be a consequence of the methodology used in constructing the GMPE: selection of the median value from an ensemble at each grid point may not reflect the actual disturbance of the front. Correlations between the OI and OSTIA FDI are of similar magnitude to those of the OEI (greater in the case of subseasonal anomalies), and the correlations for individual months are the lowest in December–April (Fig. S3).

During September–April at monthly resolution, the FDI shows no significant ($p < 0.1$) correlations with the OEI in any of the datasets. However, if the OEI and FDI are partitioned based on the negative and positive OEI phases, a different picture emerges. The positive phases of the OEI are positively correlated (OI: 0.54; GMPE: 0.59; OSTIA: 0.52) with the FDI; however, the negative phases of the OEI are negatively correlated (OI: −0.47; GMPE: −0.54; OSTIA: −0.50) with the FDI. A high FDI can thus be associated with both large positive and negative values of the OEI. The FDI increases as the OE front moves away from the climatological location in either direction. The relationship between the OEI and FDI is summarized in Fig. 5.

In February, for the lowest tercile (12 years) of the OEI difference index (Fig. 3b), six have a low FDI and one has a high FDI. Conversely, considering high tercile values, 3 of the 12 years have low FDI values and seven have high FDI values. This makes sense as a broken, less well-defined front may well be detected more ambiguously in different datasets. Additional contributions to the difference index come from the more well-defined regions of the front, where differences still occur for each time step.

Using the OI SST dataset and considering the SST gradients in February as an example (Fig. 6), the climatological mean location of the maximum SST gradient (black curve) does not coincide with the climatological February mean for the SST gradient field (shading, Fig. 6a). In the west, it lies between the two regions of strong poleward SST gradients, a consequence of the climatological location reflecting fluctuations in the relative strength of the northern and southern SST fronts. In 1991, sections of the maximum SST gradient are located well to the north and south of the climatological SST front (Fig. 6b), with the maximum around 35°N likely associated with the KE. Such a large overall disturbance results in a high FDI (1.25). In contrast, in 1995, the maximum SST gradients are close to but either side of the climatological values, with an overall more zonal location and a low FDI (0.42).

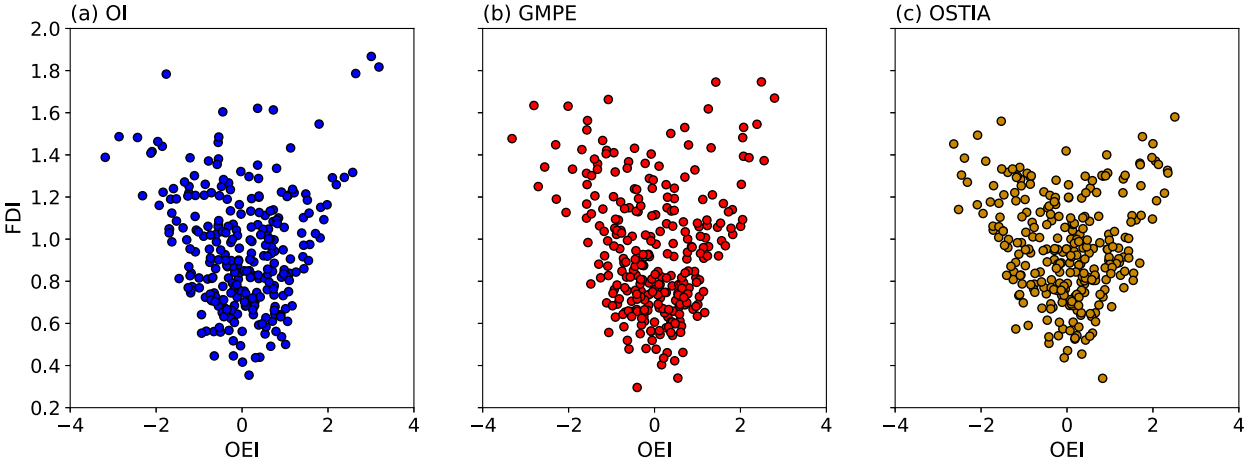

FIG. 5. Scatterplots of the monthly OEI against monthly FDI for SONDJFMA, for (a) OI, (b) GMPE, and (c) OSTIA datasets, 1982–2016.

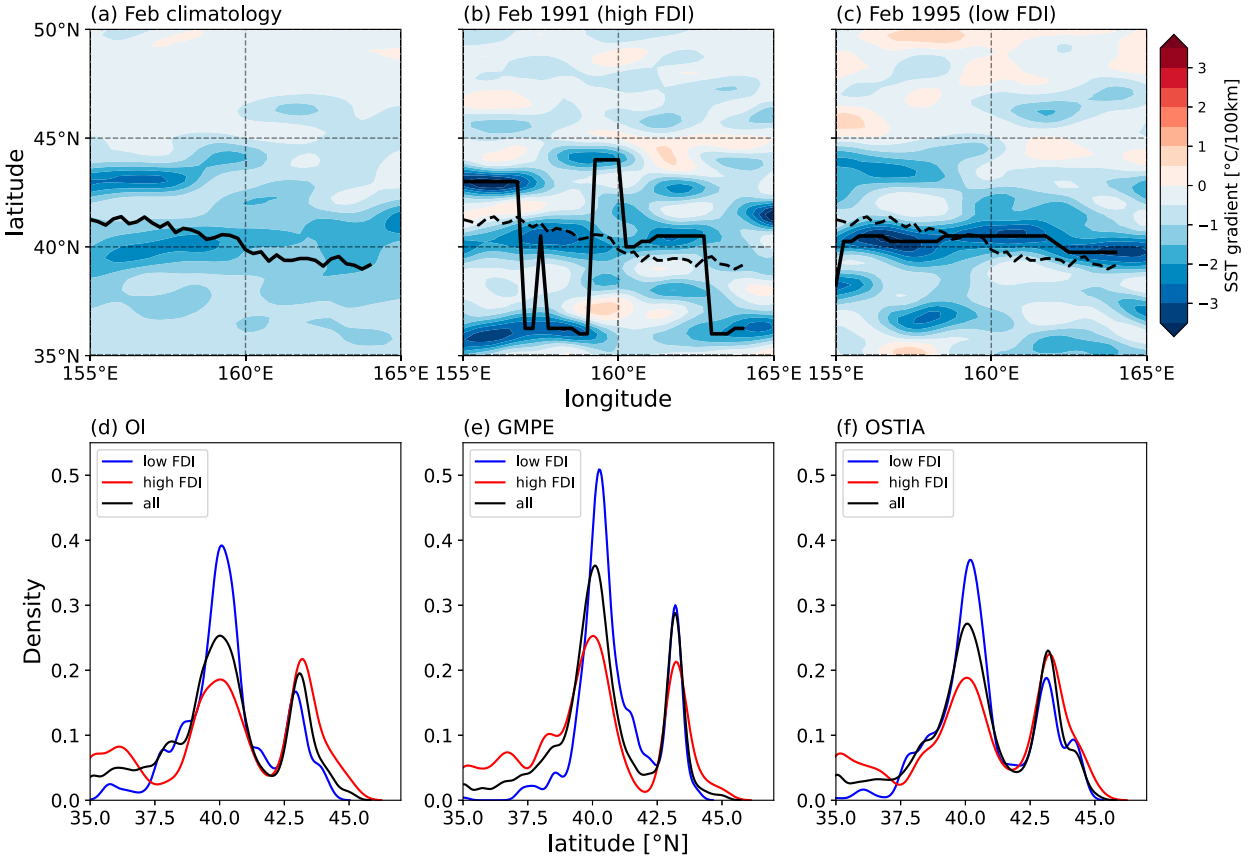

FIG. 6. February-mean poleward SST gradient (color shading; °C per 100 km) for (a) February climatology 1982–2016, (b) February 1991 (a high FDI case), and (c) February 1995 (a low FDI case) from the OI SST dataset. In (a), the locations of the maximum absolute SST gradients are shown with a black solid line which is drawn as black dashed lines in (b) and (c) extending only to 164°E (the extent of the FDI). Data are not detrended in (a)–(c). (d)–(f) Kernel density estimates of the distribution for latitudes of the February maximum absolute SST gradients, at each longitude and for each February in 1982–2016 for (d) OI, (e) GMPE, and (f) OSTIA. Blue (red) curves show the third of months with the lowest (highest) FDI, and black curve is for all the February months.

d. Physical factors associated with the FDI

The FDI is moderately associated with the magnitude of the poleward SST gradient averaged over 39°–41°N, 155°–164°E. Specifically, correlations between the FDI and SST gradient are 0.43 (OI), 0.30 (GMPE), and 0.38 (OSTIA), based on monthly data during 1982–2016. All these values are highly significant ($p < 0.01$) and indicate that a stronger (more negative) poleward temperature gradient at 40°N is associated with a lower FDI, closer to climatology. This implies a stronger SST gradient at this latitude is more likely to be selected as part of the OE front defined along the maximum absolute SST gradient. In a high FDI case (Fig. 6b), there are regions of stronger (than climatology) positive poleward SST gradients to the north and south of 40°N, whereas in the low FDI case (Fig. 6c), the gradients along 40°N are the strongest in the domain. The probability density functions in Figs. 6d–f reinforce this. There is a clear increase in occurrences of maximum SST gradients at around 40°N for low FDI months (blue lines), while for high FDI years, this frequency decreases, with increased frequency particularly at lower latitude (35°–37°N, red lines, in the KE region). There is a secondary frequency peak at around 43°N, where changes in frequency are dependent on dataset. The significant correlations between the FDI and the SST gradient magnitude at ~40°N are modest. The magnitude of the SST gradient explains only a part of the FDI, and it is likely to be a result of interactions between a range of variables related to local SST, SST gradients, and SSH gradients, some of which may be nonlinear.

Below and in section 4e, we recalculate the OI and OSTIA indices for an extended period (1982–2021). We do not extend the GMPE indices as at the time of writing, there is a gap in this dataset for much of 2017. We now consider whether mesoscale oceanic eddy activity has any influence on the FDI. The amplitude of mesoscale eddy activity is calculated from the monthly standard deviation of daily OI SST data that have been high pass filtered by application of a spatial FFT filter (section 3c; Fig. 7). There is high mesoscale eddy activity in the region between the KE and OE (~35°–40°N; Fig. 7a). In addition, there is increased eddy activity along the two quasi-stationary regions of strong SST gradient associated with the OE Front (150°–155°E, 40°–44°N, and 165°–170°E, 40°–43°N).

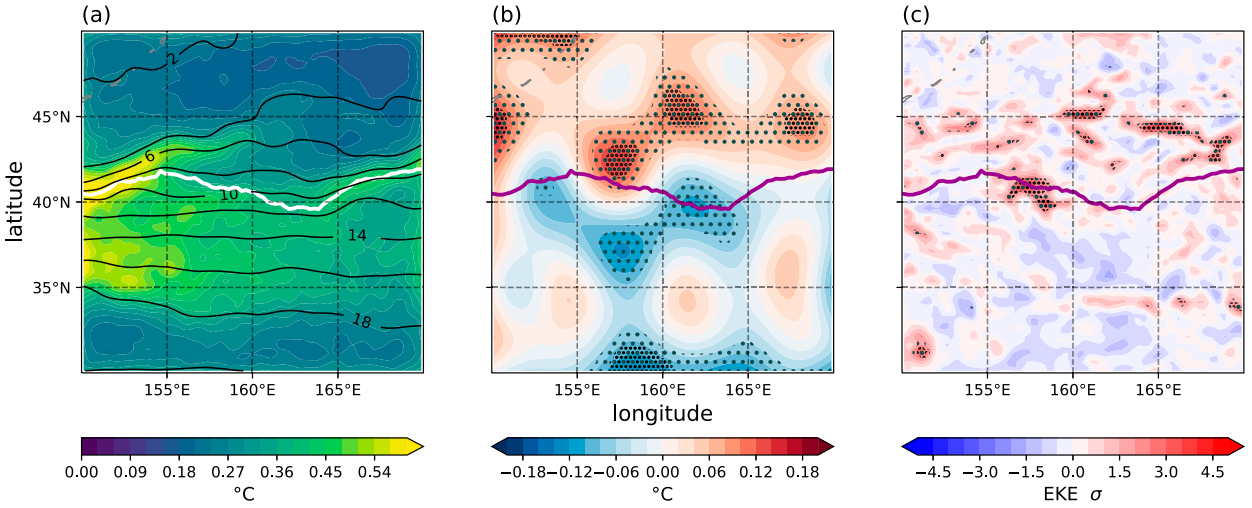

FIG. 7. (a) OI SST monthly standard deviation of spatially high-pass filtered daily data averaged over DJFM, 1982–2021. Black contours show the DJFM mean SST. (b) Monthly standard deviation of daily spatially high-pass filtered SST, with additional low-pass filter applied to the monthly standard deviations prior to regression, regressed against the OI FDI (for positive FDI months only). (c) Monthly mean EKE standardized anomalies regressed against the OI FDI (positive regression only), 1993–2021. Stippling indicates significance at $p < 0.1$ (fine black) and $p < 0.2$ (coarse gray) after the application of the FDR. The monthly SST data are detrended prior to regression. The DJFM mean location of the OE is shown in (a) white and (b),(c) magenta.

The FFT-filtered OI SST fields regressed onto the FDI for December–March (at monthly resolution) result in significantly increased mesoscale eddy energy in the positive regression (Fig. 7b) to the north of the climatological SST front. The eddy energy increase overlaps the front in the western part of the FDI domain, while it decreases in the eastern part of the front. Here, the additional low-pass filtering cleans up the very noisy high-pass-filtered fields. A similar pattern is observed using OSTIA data, although the field is noisier and results are not significant (not shown). The regressions were repeated for December–January or January–February and showed significance using both OI and OSTIA (not shown). A high FDI indicative of a more disturbed maximum SST gradient is thus associated with increased eddy activity to the north.

To confirm the association between mesoscale eddy activity near the Oyashio Extension SST front and the FDI, we regress the eddy kinetic energy (EKE) monthly mean standardized anomalies against the OI FDI (Fig. 7c). In broad agreement with the results derived from the FFT-filtered SST, albeit with less widespread statistical significance, the regression indicates increased eddy activity with increasing FDI along and to the north of the SST front for a positive FDI (the climatological mean FDI is removed to create positive and negative values). Increased eddy activity is thus associated with increased disturbance of the SST front where it is more weakly defined. Results are qualitatively similar using the OSTIA FDI or monthly standard deviation of daily standardized EKE anomalies (not shown) at each grid point, suggesting a shift in both the mean and spread of EKE with an increased FDI. A simple monthly EKE index over the northern part of the FDI domain (155°–165°E, 41°–45°N) is significantly correlated ($r = 0.48$ for OI, $r = 0.57$ for OSTIA, $p < 0.05$) with the positive phase of the FDI for January and February, indicating that a proportion of the positive FDI is explained by mesoscale eddy activity. There is no significant correlation between the EKE index and the positive phase of the OEI. While the FDI shows an association with SST mesoscale eddy activity, there is no significant association with local unfiltered SST variability (not shown).

e. *Impacts of changes in frontal disturbance*

Thus far, our focus has been on the mesoscale (SST fronts and mesoscale eddy activity in the Oyashio Extension region). We now address whether the variability of the FDI and OEI is manifested in large-scale atmospheric fields over a North Pacific domain (140°–240°E, 30°–60°N) by regressing the various storm-track metrics and SLP against the FDI, using the extended period to 2021. We examine significant regressions at 1-month lag between the respective FDI and OEI in January and February (JF) and the February and March (FM) atmospheric fields, at monthly resolution. This time lag is chosen to capture the influence of the changes in frontal disturbance or OE shift on the atmosphere, avoiding atmospheric influences on the ocean which dominate at zero lag. Our focus is on winter, when turbulent surface heat exchanges are strongest and the mean position of the storm track is more closely aligned with the oceanic fronts. Significant changes can also be observed at longer lags (not shown); however, we do not aim to be exhaustive here. We focus on a small number of metrics for clarity and also average the indices from the OI and OSTIA datasets, to reduce noise.

Symmetric and asymmetric regression results are summarized in Fig. 8, with statistical significance at $p < 0.1$ and $p < 0.2$ indicated by dark and light blue shading, respectively, where significance after adjusting with the FDR is considered downstream

(a) FDI dataset JF	February-March atmospheric field																				
	300hPa v′v′			850hPa v′T′			500hPa omega SD highpass			850hPa v wind diffs SD			Total Precip. diffs SD			800hPa Eady Growth Rate			SLP		
	+	-	s	+	-	s	+	-	s	+	-	s	+	-	s	+	-	s	+	-	s
OI																					
OSTIA																					
MEAN																					
Significance Agreement score	0	0	0	0	0	0	3	0	3	3	0	2	0	0	3	0	3	0	2	0	3
Spatial correlation	0.53	0.58	0.93	0.28	0.19	0.86	0.72	0.59	0.89	0.49	0.39	0.83	0.76	0.45	0.91	0.71	0.31	0.84	0.86	0.73	0.93

(b) OEI dataset JF	February-March atmospheric field																				
	300hPa v′v′			850hPa v′T′			500hPa omega SD highpass			850hPa v wind diffs SD			Total Precip. diffs SD			800hPa Eady Growth Rate			SLP		
	+	-	s	+	-	s	+	-	s	+	-	s	+	-	s	+	-	s	+	-	s
OI																					
OSTIA																					
MEAN																					
Significance Agreement score	0	0	0	0	0	0	0	0	0	0	0	0	0	0	0	0	0	0	0	0	0
Spatial correlation	0.23	0.58	0.54	0.35	0.18	0.66	0.71	0.47	0.59	0.80	0.49	0.64	0.63	0.44	0.66	0.78	0.47	0.35	0.97	0.30	0.64

FIG. 8. Grid showing where significant regression coefficients occur in the 160°E–140°W, 30°–55°N region of regression maps of (a) the JF FDI and (b) the JF OEI, for indices derived from each dataset against atmospheric and storm-track variables. The symbols +, −, and *s* denote positive, negative, and symmetric regression cases, respectively. Light blue indicates that the regression map shows regions of significance at $p < 0.2$, and dark blue indicates that there is significance at $p < 0.1$, after application of the FDR. SD = monthly standard deviation of daily high-pass-filtered or daily-differenced data.

of the OE front (160°E–140°W, 30°–55°N). Recall that for these regressions, we remove the climatological mean FDI to create positive and negative values. There are fewer significant regressions for negative FDI (little OE disturbance) but more frequent ones for the positive FDI (strong OE disturbances), while the FDI also frequently exhibits significant symmetric associations with the atmospheric variables. For the OEI, all but one of the significant regressions are for positive OEIs. The only significance for the negative OEI occurs for the meridional winds. Overall, the asymmetric regressions on OEIs are too weak to lead to significant symmetric regressions.

A simple score quantifies the agreement of any statistical significance between datasets for each index: if indices from both datasets (excluding the mean index calculated as the average of the OI and OSTIA indices) show significant positive associations with an atmospheric variable, a score of two is awarded for a $p < 0.1$ significance level and one for a $p < 0.2$ level. There is no agreement of significance between the OSTIA and OI OEI. The weaker regressions onto OEIs may mean any signal is hard to separate from noise, hence the reduced significance. Spatial correlations indicate the spatial degree of similarity between regressions for each index, derived from different datasets. While there is relatively little difference between these correlations for positive and negative regressions, the symmetric regressions for the FDI have a spatial correlation consistently 0.19–0.49 higher than the equivalent regression of OEI.

All calculated regression maps for indices from both datasets are shown in Figs. S4–S9. Here, we present the regression maps for the OEI using the mean OEI averaged over two datasets (Fig. 9). All significant regressions occur for the positive regression case, when the OE is shifted northward, with the exception of a significant negative regression for meridional wind differences (Fig. 8b). A significant ($p < 0.1$) low SLP anomaly monopole is centered over the Aleutian Islands (Fig. 9a), and significant regression coefficients for the storm-track metrics occur consistently on the southern flank of the low pressure anomalies: a northward shift of the OE is associated 1 month later with increases in the standard deviation of meridional wind and total precipitation daily differences and an increase in 800-hPa EGR, mainly between 180° and 140°W (Figs. 9b–d). This indicates an eastward extension of storm-track activity downstream of the OE. The daily-differenced parameters are associated with the transit of low pressure systems along the storm track. The increased variability reflects the increased passage of fronts or stronger storms, which are accompanied by changes in wind direction, and the warm and cold sectors, where rainfall and meridional winds are more vigorous and more changeable.

For the regression maps using the FDI (Fig. 10), the low pressure anomaly is centered around 5° further south than for the OEI (Fig. 10a). In addition, there is significance ($p < 0.1$) for positive regressions with 500-hPa omega (Fig. 10b) between 180° and 140°W. Descending cold air (positive omega) is associated with the cold sector behind the cold front, and ascending warm air (negative omega) is linked to the warm front ahead of the warm sector, which will combine to increase variability of omega when storm-track activity increases.

An increase in SST front disturbance from climatology (a positive FDI) is associated with a southward-shifted low pressure monopole (relative to the OEI) a month later, with increased storm-track activity to the south of the monopole.

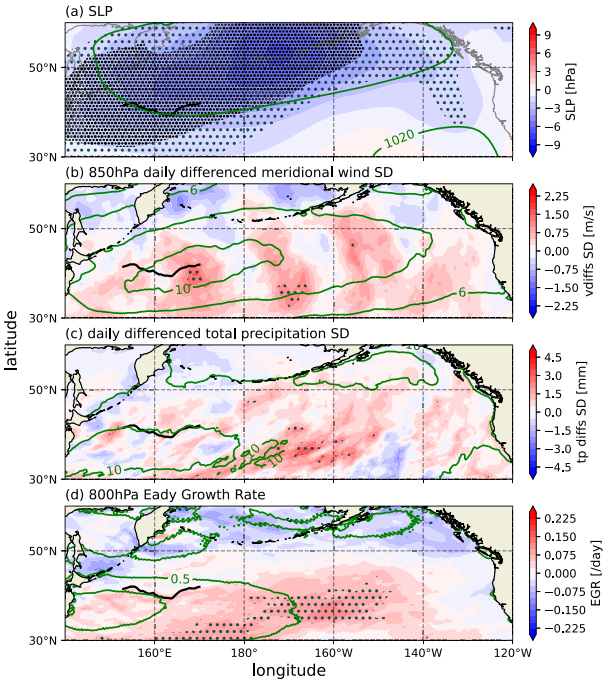

FIG. 9. Asymmetric (positive) regression on the dataset-averaged OEI, 153°–173°E for JF, for various FM atmospheric fields related to storm tracks. Maps are only shown where there are significant regression coefficients ($p < 0.2$), after the FDR is applied. Shading shows significance at $p < 0.2$ (coarse gray) or $p < 0.1$ (fine black). The solid black line shows the mean position of the OE front. Green contours show the climatological mean values of the respective atmospheric field. Contour intervals: 10 hPa (SLP); 2 m s^{-1} (v wind differences); 5 mm (total precipitation differences); 0.25 day^{-1} (EGR).

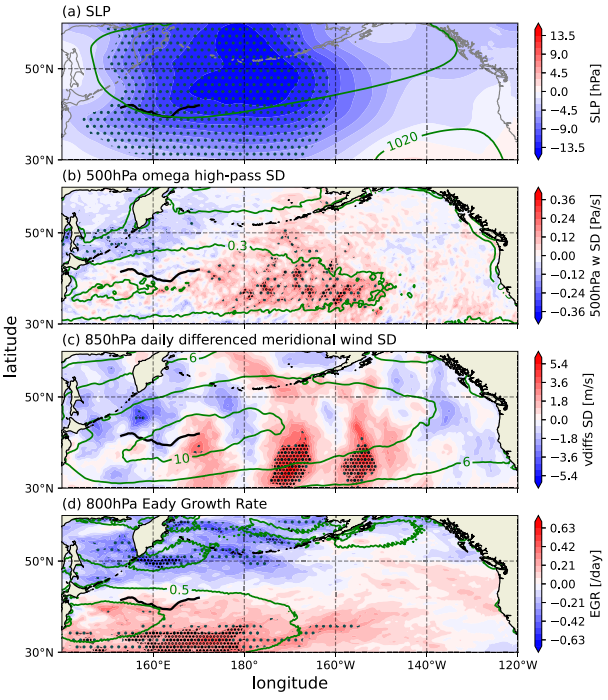

FIG. 10. As in Fig. 9, except that regressions are on the positive values of the average FDI. Note that the color bar scales are different from those in Fig. 9. Climatological 500-hPa omega high-pass-filtered SD contour interval: 0.1 Pa s^{-1} (green contours).

The increase in EGR and meridional wind differences is on the southern flank of the climatological storm track. Interestingly, there are no significant regressions for either 300 $v'v'$ or 850-hPa $v'T'$ using the averaged indices, although we only consider a 1-month lag for specific months.

Significant negative regressions are found when the EGR is regressed onto the average FDI, using the time steps where the FDI is negative (Fig. S10e). As the FDI becomes less negative (shifts away from climatological frontal position), EGR increases in the Eastern Pacific, but then as the FDI becomes positive (more strongly disturbed), the EGR increase shifts to the south (Fig. 10). In addition, many atmospheric variables show a significant symmetric response to the average FDI (Figs. S10a–d). An increase in SLP in the eastern Pacific at around 30°N is associated with a poleward shift of significant storm-track responses.

Whereas the spatial patterns of significant regression coefficients for the OEI and FDI in positive regression show an eastward extension of the storm track (Figs. 9 and 10), the FDI responses are also shifted to the south. As discussed in section 4c, the positive phases of the FDI and OEI are significantly positively correlated (r = 0.52–0.59), suggesting that the atmospheric response to each time series in this phase would show some similarities.

As seen in section 4d, the FDI is an indicator of ocean mesoscale eddy variability, so an increase in mesoscale eddy activity poleward of 40°N in the central OE region is associated with increased storm-track activity. The regressions of the positive phase of the EKE index (section 4d) for the storm-track metrics and SLP indicate significant downstream responses (Fig. S11). It is notable that significant responses are strong, even over the shorter time period available for the EKE index (1993–2021), and extend further downstream to the east Pacific.

5. Discussion and summary

We have shown that certain features of the OEI and subsequent regressions with atmospheric fields are dataset dependent. Dataset selection is therefore an important aspect of a study's design, and we would recommend considering more than one dataset, along with using different metrics for quantifying the SST fronts, to identify the robust features of air–sea interactions. SSTs used in ERA5 in particular appear to be an outlier, showing weaker correlations with indices from other datasets, and markedly different responses in regression maps. On average, ERA5 underestimates the SST variability in the KE region compared with an ensemble median of SST datasets (Yang et al. 2021). These WBC regions have higher mesoscale eddy activity, and it is possible that the SSTs used in ERA5 underestimate the SST fluctuations in this region (Sroka et al. 2022). Calculating the amplitude of the SST

mesoscale eddy activity for ERA5, as for Fig. 7a, confirms this (not shown). As ERA5 uses HadISST2.0 data prior to 2007, and OSTIA thereafter, this discontinuity could be a cause of the discrepancy between ERA5 and the other datasets.

It is commonplace to use different SST datasets with atmospheric variables from a reanalysis such as ERA5. In reanalyses, SST is a boundary condition and the lower-tropospheric variables used here are likely primarily constrained by atmospheric data. The partitioning of the influence of the atmospheric data and SST boundary conditions is difficult to quantify. However, the impact of SSTs may be greater for the surface heat fluxes and precipitation, which are less well constrained by observations, which should be borne in mind when performing such analyses.

Differences in the representation of the OEI between datasets result from different representations of the SST gradient, particularly in the relatively weak central portion of the SST front. The FDI is a novel index designed to quantify the disturbance of the maximum SST gradient in the central section of the OE.

The association of positive FDI with mesoscale eddy variability is interesting but cannot be easily explained within the scope of this paper. Eddies can erode the SST front through increased surface heat loss (e.g., Nonaka et al. 2009). However, recent studies indicate that eddies may also act to maintain SST fronts, through vertical heat transport replenishing the heat lost from the surface (Jing et al. 2020). Tang et al. (2022) report that most eddies weaken the SST gradient within the eddies, but induce the redistribution of the SST front in the surrounding ocean, which varies according to whether eddies are cyclonic or anticyclonic. Kuwano-Yoshida and Minobe (2017) using a model experiment showed that decreased SST gradients can induce an eastward extension of storm-track activity over the North Pacific. This is consistent with the southeastward increase of storm-track activity found for positive FDI and associated mesoscale activity and reduced SST gradient. There is also a southward displacement of the storm-track response to the positive FDI. This is similar to the results of Gan et al. (2023), where mesoscale ocean eddy activity in the downstream KE region is associated with ocean warming, inducing surface wind convergence and upward motion. Increased fine-scale diabatic heating in the lower troposphere and moisture supply from the warmer water below enhances updrafts which cool the midtroposphere. Background northwesterly winds spread the cooling with an associated southward displacement of atmospheric synoptic eddy activity. A similar mechanism may apply in our study with enhanced ocean eddy activity in the OE region. In contrast to our results, Ma et al. (2017) find that a southward shift in the storm track is associated with removing mesoscale eddy activity in the KE region; however, their focus is a much broader region over the KOE domain whereas our focus is near and to the north of the OE.

The increased mesoscale eddy activity to the north of the OE front and increased FDI are associated with increased storm-track activity one month later. This is consistent with previous model results (Jia et al. 2019) where atmospheric baroclinic growth is modified via the presence of oceanic eddies. This results in increased moisture content in the marine atmospheric boundary layer and possibly enhanced cyclogenesis via moist baroclinic instability. The origins of this eddy activity have not been determined and will be left for future research; however, there may be links with KE variability (Fig. S12 suggests that a high FDI is associated with increased meandering in the upstream portion of the KE, while the low FDI is associated with a more zonal, less meandering flow) and the strength of the Isoguchi jets (Isoguchi et al. 2006; Seo et al. 2014; Sugimoto and Hanawa 2011; Sugimoto 2014).

We have found that the storm-track responses associated with the OE have a significant asymmetric component. The positive regression phase for OEI and FDI shows some similarities, and the time series show moderate positive correlations in the positive phase. Both the northward shift of the OE in its positive phase and the increasing shift away from the climatological front position for the FDI are associated with increased downstream storm-track activity and a monopole of low pressure near the Aleutian Islands. In the case of the OEI, the storm track extends eastward, whereas for the FDI, there is also a southward shift. The significant impact of the northward shift of the OE (a more positive OEI) can be understood in the context of storm tracks being anchored on the northern flanks of SST fronts; high baroclinicity is maintained by the contrast in heat supply across the SST front (e.g., Nakamura et al. 2008), so that shifts in the SST fronts will have an impact on the storm track.

The OEI appears to perform poorly as a measure of high-frequency (i.e., storm-track-related) air–sea interaction using a 1-month lag between the OEI and the subsequent storm-track variable and when considering consistency of any statistical significance between datasets. Previous research has identified more significant air–sea interactions than found here due to different research foci. For example, Frankignoul et al. (2011) examine the OEI in the context of large-scale atmospheric variability. Indeed, their results are consistent with those presented here as they find little significance at 1-month lag, but there were stronger signals at lags of 2–5 months. In addition, our focus is winter, whereas Frankignoul et al. (2011) find a strong response based on all months as well as with an August–October index and November–January atmospheric fields. Using our approach, we indeed find significant responses to the OEI at lags over these longer periods, both symmetric and asymmetric (not shown). Furthermore, Frankignoul et al. (2011) consider a different time period (1982–2008) and use different datasets, both of which can contribute to differences in results (cf. Zhou and Cheng 2021).

The growth in high-frequency weather systems as indicated by the storm-track response may subsequently lead to changes in diabatic heating and momentum and heat fluxes by these high-frequency systems, with subsequent changes in the jet stream. However, in the present study, we do not consider the FDI impacts at different lag times which may reveal such responses. Neither do we compare early and late winter differences, or differences at other times in the year. Investigating the physical mechanisms which link fluctuations in the positive FDI to changes in the storm track is also left for future research. Here, we simply present the FDI as a complementary approach to identifying high-frequency air–sea

interactions, which at short time scales with a lag of around 1 month produces consistent large-scale atmospheric responses when using different datasets to derive the index.

The key findings of the study are summarized below:

1) The OEIs obtained from different datasets show considerable variation. Correlations are stronger on seasonal time scales but weak on a subseasonal scale. We do not recommend using indices such as the OEI for identifying subseasonal variability in air–sea interactions, due to the large discrepancies between datasets at this temporal scale. Identifying a single best dataset to use for defining the OEI is not clearly achievable.
2) These differences arise from slight differences in the representation of SST gradients in the considered datasets, particularly in the more complex central regions where there are parallel fronts or fronts are weak.
3) We develop a new index, the FDI, to quantify the complex central region of the OE and the extent to which the SST gradient deviates from climatology. This new index is associated with the strength of the SST gradient at 40°N. This gradient is in turn affected by fluctuations in ocean mesoscale eddy activity to the north and south. It can be used to identify air–sea interactions at shorter time lags than the OEI and is an indicator of mesoscale eddy activity in the OE region.
4) The FDI has both symmetric and asymmetric associations with storm-track responses. When the average deviation from climatology is high, a further increase in disturbance is associated with an eastward extension and southward shift of the storm track. These responses are linked to ocean mesoscale eddy activity in the region.
5) Similarly, the response of storm-track metrics to the north–south shifts of the OE front (the OE index) is asymmetric. It is the positive regression phase that shows most significance (when the OE front is shifted to the north).
6) The FDI produces a more robust air–sea interaction signal with storm-track metrics than the OEI, for the 1-month time lag considered here, as there is more agreement in statistical significance between the regressions based on indices calculated from the different SST datasets and the significance of the regressions is often at a higher threshold. The reason for the difference between the OEI and FDI in terms of the time taken for significant responses to emerge needs to be investigated in a future study. It seems that at a 1-month lag, the OEI response is too weak to achieve consistent statistical significance.

Acknowledgments. The authors acknowledge support from the NSFGEO-NERC project "Large-scale atmospheric circulation response to Oyashio Extension frontal variability," Award AGS-2040073. The National Center for Atmospheric Research (NCAR) is a major facility sponsored by the U.S. National Science Foundation (NSF) under Cooperative Agreement 1852977. We thank the reviewers for their thoughtful comments which have improved the manuscript.

Data availability statement. All data used in this study are available online.

REFERENCES

Banzon, V., T. M. Smith, T. M. Chin, C. Liu, and W. Hankins, 2016: A long-term record of blended satellite and in situ sea-surface temperature for climate monitoring, modeling and environmental studies. *Earth Syst. Sci. Data*, **8**, 165–176, https://doi.org/10.5194/essd-8-165-2016.

Benjamini, Y., and Y. Hochberg, 1995: Controlling the false discovery rate: A practical and powerful approach to multiple testing. *J. Roy. Stat. Soc.*, **57B**, 289–300, https://doi.org/10.1111/j.2517-6161.1995.tb02031.x.

Czaja, A., C. Frankignoul, S. Minobe, and B. Vannière, 2019: Simulating the midlatitude atmospheric circulation: What might we gain from high-resolution modeling of air-sea interactions? *Curr. Climate Change Rep.*, **5**, 390–406, https://doi.org/10.1007/s40641-019-00148-5.

Donlon, C. J., M. Martin, J. Stark, J. Roberts-Jones, E. Fiedler, and W. Wimmer, 2012: The Operational Sea Surface Temperature and Sea Ice Analysis (OSTIA) system. *Remote Sens. Environ.*, **116**, 140–158, https://doi.org/10.1016/j.rse.2010.10.017.

Fiedler, E. K., and Coauthors, 2019: Intercomparison of long-term sea surface temperature analyses using the GHRSST Multi-Product Ensemble (GMPE) system. *Remote Sens. Environ.*, **222**, 18–33, https://doi.org/10.1016/j.rse.2018.12.015.

Frankignoul, C., and Y.-O. Kwon, 2022: On the statistical estimation of asymmetrical relationship between two climate variables. *Geophys. Res. Lett.*, **49**, e2022GL100777, https://doi.org/10.1029/2022GL100777.

——, N. Sennéchael, Y.-O. Kwon, and M. A. Alexander, 2011: Influence of the meridional shifts of the Kuroshio and the Oyashio Extensions on the atmospheric circulation. *J. Climate*, **24**, 762–777, https://doi.org/10.1175/2010JCLI3731.1.

Gan, B., T. Wang, L. Wu, J. Li, B. Qiu, H. Yang, and L. Zhang, 2023: A mesoscale ocean–atmosphere coupled pathway for decadal variability of the Kuroshio Extension system. *J. Climate*, **36**, 485–510, https://doi.org/10.1175/JCLI-D-21-0557.1.

Good, S., and Coauthors, 2020: The current configuration of the OSTIA system for operational production of foundation sea surface temperature and ice concentration analyses. *Remote Sens.*, **12**, 720, https://doi.org/10.3390/rs12040720.

Hersbach, H., and Coauthors, 2020: The ERA5 global reanalysis. *Quart. J. Roy. Meteor. Soc.*, **146**, 1999–2049, https://doi.org/10.1002/qj.3803.

Hoskins, B. J., and P. J. Valdes, 1990: On the existence of storm-tracks. *J. Atmos. Sci.*, **47**, 1854–1864, https://doi.org/10.1175/1520-0469(1990)047<1854:OTEOST>2.0.CO;2.

Huang, B., C. Liu, E. Freeman, G. Graham, T. Smith, and H.-M. Zhang, 2021: Assessment and intercomparison of NOAA Daily Optimum Interpolation Sea Surface Temperature (DOISST) version 2.1. *J. Climate*, **34**, 7421–7441, https://doi.org/10.1175/JCLI-D-21-0001.1.

Isoguchi, O., H. Kawamura, and E. Oka, 2006: Quasi-stationary jets transporting surface warm waters across the transition zone between the subtropical and the subarctic gyres in the North Pacific. *J. Geophys. Res.*, **111**, C10003, https://doi.org/10.1029/2005JC003402.

Jia, Y., P. Chang, I. Szunyogh, R. Saravanan, and J. T. Bacmeister, 2019: A modeling strategy for the investigation of the effect of mesoscale SST variability on atmospheric dynamics. *Geophys. Res. Lett.*, **46**, 3982–3989, https://doi.org/10.1029/2019GL081960.

Jing, Z., and Coauthors, 2020: Maintenance of mid-latitude oceanic fronts by mesoscale eddies. *Sci. Adv.*, **6**, eaba7880, https://doi.org/10.1126/sciadv.aba7880.

Kida, S., and Coauthors, 2015: Oceanic fronts and jets around Japan: A review. *J. Oceanogr.*, **71**, 469–497, https://doi.org/10.1007/s10872-015-0283-7.

Kuwano-Yoshida, A., and S. Minobe, 2017: Storm-track response to SST fronts in the northwestern Pacific region in an AGCM. *J. Climate*, **30**, 1081–1102, https://doi.org/10.1175/JCLI-D-16-0331.1.

Kwon, Y.-O., M. A. Alexander, N. A. Bond, C. Frankignoul, H. Nakamura, B. Qiu, and L. A. Thompson, 2010: Role of the Gulf Stream and Kuroshio–Oyashio Systems in large-scale atmosphere–ocean interaction: A review. *J. Climate*, **23**, 3249–3281, https://doi.org/10.1175/2010JCLI3343.1.

Ma, X., P. Chang, R. Saravanan, R. Montuoro, H. Nakamura, D. Wu, X. Lin, and L. Wu, 2017: Importance of resolving Kuroshio Front and eddy influence in simulating the North Pacific storm track. *J. Climate*, **30**, 1861–1880, https://doi.org/10.1175/JCLI-D-16-0154.1.

Martin, M., and Coauthors, 2012: Group for High Resolution sea surface temperature (GHRSST) analysis fields intercomparisons. Part 1: A GHRSST Multi-Product Ensemble (GMPE). *Deep-Sea Res. II*, **77–80**, 21–30, https://doi.org/10.1016/j.dsr2.2012.04.013.

Nakamura, H., T. Sampe, Y. Tanimoto, and A. Shimpo, 2004: Observed associations among storm tracks, jet streams and midlatitude oceanic fronts. *Earth's Climate: The Ocean-Atmosphere Interaction, Geophys. Monogr.*, Vol. **147**, Amer. Geophys. Union, 329–346, https://doi.org/10.1029/147GM18.

——, ——, A. Goto, W. Ohfuchi, and S.-P. Xie, 2008: On the importance of midlatitude oceanic frontal zones for the mean state and dominant variability in the tropospheric circulation. *Geophys. Res. Lett.*, **35**, L15709, https://doi.org/10.1029/2008GL034010.

Nonaka, M., H. Nakamura, B. Taguchi, N. Komori, A. Kuwano-Yoshida, and K. Takaya, 2009: Air–sea heat exchanges characteristic of a prominent midlatitude oceanic front in the South Indian Ocean as simulated in a high-resolution coupled GCM. *J. Climate*, **22**, 6515–6535, https://doi.org/10.1175/2009JCLI2960.1.

Qiu, B., 2019: Kuroshio and Oyashio currents. *Encyclopedia of Ocean Sciences*, 3rd ed. J. K. Cochran, H. J. Bokuniewicz, and P. L. Yager, Eds., Academic Press, 384–394, https://doi.org/10.1016/B978-0-12-409548-9.11295-3.

——, S. Chen, and N. Schneider, 2017: Dynamical links between the decadal variability of the Oyashio and Kuroshio Extensions. *J. Climate*, **30**, 9591–9605, https://doi.org/10.1175/JCLI-D-17-0397.1.

Révelard, A., C. Frankignoul, N. Sennéchael, Y.-O. Kwon, and B. Qiu, 2016: Influence of the decadal variability of the Kuroshio Extension on the atmospheric circulation in the cold season. *J. Climate*, **29**, 2123–2144, https://doi.org/10.1175/JCLI-D-15-0511.1.

——, ——, and Y.-O. Kwon, 2018: A multivariate estimate of the cold season atmospheric response to North Pacific SST variability. *J. Climate*, **31**, 2771–2796, https://doi.org/10.1175/JCLI-D-17-0061.1.

Reynolds, R. W., T. M. Smith, C. Liu, D. B. Chelton, K. S. Casey, and M. G. Schlax, 2007: Daily high-resolution-blended analyses for sea surface temperature. *J. Climate*, **20**, 5473–5496, https://doi.org/10.1175/2007JCLI1824.1.

Sampe, T., H. Nakamura, A. Goto, and W. Ohfuchi, 2010: Significance of a midlatitude SST frontal zone in the formation of a storm track and an eddy-driven westerly jet. *J. Climate*, **23**, 1793–1814, https://doi.org/10.1175/2009JCLI3163.1.

Seo, H., and Coauthors, 2023: Ocean mesoscale and frontal-scale ocean–atmosphere interactions and influence on large-scale climate: A review. *J. Climate*, **36**, 1981–2013, https://doi.org/10.1175/JCLI-D-21-0982.1.

Seo, Y., S. Sugimoto, and K. Hanawa, 2014: Long-term variations of the Kuroshio Extension path in winter: Meridional movement and path state change. *J. Climate*, **27**, 5929–5940, https://doi.org/10.1175/JCLI-D-13-00641.1.

Small, R. J., and Coauthors, 2008: Air–sea interaction over ocean fronts and eddies. *Dyn. Atmos. Oceans*, **45**, 274–319, https://doi.org/10.1016/j.dynatmoce.2008.01.001.

——, R. A. Tomas, and F. O. Bryan, 2014: Storm track response to ocean fronts in a global high-resolution climate model. *Climate Dyn.*, **43**, 805–828, https://doi.org/10.1007/s00382-013-1980-9.

——, R. Msadek, Y.-O. Kwon, J. F. Booth, and C. Zarzycki, 2019: Atmosphere surface storm track response to resolved ocean mesoscale in two sets of global climate model experiments. *Climate Dyn.*, **52**, 2067–2089, https://doi.org/10.1007/s00382-018-4237-9.

Smirnov, D., M. Newman, M. A. Alexander, Y.-O. Kwon, and C. Frankignoul, 2015: Investigating the local atmospheric response to a realistic shift in the Oyashio sea surface temperature front. *J. Climate*, **28**, 1126–1147, https://doi.org/10.1175/JCLI-D-14-00285.1.

Sroka, S., A. Czaja, and S. Chakravorty, 2022: Assessing the importance of mesoscale sea-surface temperature variations for surface turbulent cooling of the Kuroshio Extension in wintertime. *Quart. J. Roy. Meteor. Soc.*, **148**, 2742–2754, https://doi.org/10.1002/qj.4333.

Sugimoto, S., 2014: Influence of SST anomalies on winter turbulent heat fluxes in the eastern Kuroshio–Oyashio confluence region. *J. Climate*, **27**, 9349–9358, https://doi.org/10.1175/JCLI-D-14-00195.1.

——, and K. Hanawa, 2011: Roles of SST anomalies on the wintertime turbulent heat fluxes in the Kuroshio–Oyashio Confluence Region: Influences of warm eddies detached from the Kuroshio Extension. *J. Climate*, **24**, 6551–6561, https://doi.org/10.1175/2011JCLI4023.1.

Taguchi, B., H. Nakamura, M. Nonaka, N. Komori, A. Kuwano-Yoshida, K. Takaya, and A. Goto, 2012: Seasonal evolutions of atmospheric response to decadal SST anomalies in the North Pacific subarctic frontal zone: Observations and a coupled model simulation. *J. Climate*, **25**, 111–139, https://doi.org/10.1175/JCLI-D-11-00046.1.

Tang, R., Y. Yu, J. Xi, W. Ma, and Y. Wang, 2022: Mesoscale eddies induce variability in the sea surface temperature gradient in the Kuroshio Extension. *Front. Mar. Sci.*, **9**, 926954, https://doi.org/10.3389/fmars.2022.926954.

Wald, A., 1943: Tests of statistical hypotheses concerning several parameters when the number of observations is large. *Trans. Amer. Math. Soc.*, **54**, 426–482, https://doi.org/10.1090/S0002-9947-1943-0012401-3.

Wallace, J. M., G.-H. Lim, and M. L. Blackmon, 1988: Relationship between cyclone tracks, anticyclone tracks and baroclinic waveguides. *J. Atmos. Sci.*, **45**, 439–462, https://doi.org/10.1175/1520-0469(1988)045<0439:RBCTAT>2.0.CO;2.

Wang, Y., R. Tang, Y. Yu, and F. Ji, 2021: Variability in the sea surface temperature gradient and its impacts on chlorophyll-a

concentration in the Kuroshio extension. *Remote Sens.*, **13**, 888, https://doi.org/10.3390/rs13050888.

Wilks, D. S., 2016: "The stippling shows statistically significant grid points": How research results are routinely overstated and overinterpreted, and what to do about it. *Bull. Amer. Meteor. Soc.*, **97**, 2263–2273, https://doi.org/10.1175/BAMS-D-15-00267.1.

Wills, S. M., and D. W. J. Thompson, 2018: On the observed relationships between wintertime variability in Kuroshio–Oyashio Extension sea surface temperatures and the atmospheric circulation over the North Pacific. *J. Climate*, **31**, 4669–4681, https://doi.org/10.1175/JCLI-D-17-0343.1.

Wu, B., X. Lin, and B. Qiu, 2018: Meridional shift of the Oyashio Extension front in the past 36 years. *Geophys. Res. Lett.*, **45**, 9042–9048, https://doi.org/10.1029/2018GL078433.

Yang, C., and Coauthors, 2021: Sea surface temperature intercomparison in the framework of the Copernicus Climate Change Service (C3S). *J. Climate*, **34**, 5257–5283, https://doi.org/10.1175/JCLI-D-20-0793.1.

Yao, Y., Z. Zhong, and X.-Q. Yang, 2018a: Influence of the subarctic front intensity on the midwinter suppression of the North Pacific storm track. *Dyn. Atmos. Oceans*, **81**, 63–72, https://doi.org/10.1016/j.dynatmoce.2018.01.001.

——, ——, ——, and X. Huang, 2018b: Seasonal variation of the North Pacific storm-track relationship with the subarctic frontal zone intensity. *Dyn. Atmos. Oceans*, **83**, 75–82, https://doi.org/10.1016/j.dynatmoce.2018.06.003.

Yasuda, I., 2003: Hydrographic structure and variability in the Kuroshio-Oyashio Transition Area. *J. Oceanogr.*, **59**, 389–402, https://doi.org/10.1023/A:1025580313836.

Yook, S., D. W. J. Thompson, L. Sun, and C. Patrizio, 2022: The simulated atmospheric response to western North Pacific sea surface temperature anomalies. *J. Climate*, **35**, 3335–3352, https://doi.org/10.1175/JCLI-D-21-0371.1.

Zhou, G. D., and X. H. Cheng, 2021: Impacts of oceanic fronts and eddies in the Kuroshio-Oyashio Extension region on the atmospheric general circulation and storm track. *Adv. Atmos. Sci.*, **39**, 22–54, https://doi.org/10.1007/s00376-021-0408-4.